

Photonic Crystal Distributed Feedback Fiber Lasers with Bragg Gratings

Thomas Søndergaard

Abstract—Two new types of optical fibers, where air-holes are running down their length, are considered for making fiber lasers with Bragg gratings. The mode areas for pump and signal in these fiber lasers may be either larger or smaller compared to the corresponding mode areas for fiber lasers based on standard step index fibers. This makes possible realization of fiber lasers with a low pump threshold (small mode area), and fiber lasers suitable for high-power applications (large mode area).

Index Terms—Distributed feedback (DFB) lasers, integrated optics, optical fiber lasers, periodic structures, photonic crystals.

I. INTRODUCTION

IN THE recent few years a new class of optical fibers based on photonic crystal technology has been suggested in the literature [1]–[11]. In these fibers the single-mode properties and the intensity distribution for the guided modes differs considerably from the standard step-index fiber. In particular, it is possible to design single-mode fibers (SMF's) where the mode area for the guided mode is significantly different in size relative to that in a standard step-index fiber. As the mode area is altered the local intensity of the mode near an active medium, such as Er^{3+} -ions, is altered too. This opens up for the possibility of altered light-matter interaction between the guided modes and an active medium in the fiber. Fiber lasers with a small mode area are interesting for obtaining a low threshold, whereas lasers with a large mode area are interesting for applications where high powers are desired.

A large-mode area optical fiber based on photonic crystal technology has recently been demonstrated experimentally [4], and indeed the experimentally demonstrated honeycomb fiber [5] is suitable for reducing the mode area. In this paper the spatial mode intensity profiles at the signal wavelength (1560 nm) and pump wavelength (980 nm) relevant for two photonic crystal distributed feedback fiber laser designs are calculated. The photonic crystal fibers considered are chosen in such a way that they are single-moded at both signal and pump wavelengths. Mode intensity profiles and single-mode properties are investigated numerically using a full-vector approach based on plane-wave expansion theory and a variational principle [12]–[14]. A different full-vector method for modeling of photonic crystal fibers appears in [15].

Fiber lasers, where the design is based on doping photonic crystal fibers with Er^{3+} and writing a Bragg grating, are investigated using coupled-wave theory [16], a transfer-matrix approach [17], [18] and a model for gain provided by Er^{3+} [18], [19]. Compared to the one-dimensional model for gain used in [18] a more general model is used in this paper taking into account the distribution of signal and pump power relative to the distribution and inversion of Er^{3+} across the fiber and along the fiber.

This paper is organized in the following way. In Section II single-mode properties and field intensity profiles are considered for two fiber designs. Section III describes the transfer-matrix method and the model for gain used in this paper to calculate steady-state solutions for distributed feedback photonic crystal fiber lasers. Numerical results are presented for the two fiber laser designs in Section IV. A conclusion is given in Section V.

II. SINGLE-MODE RANGE OF WAVELENGTHS AND FIELD INTENSITY PROFILES

In this section the single-mode properties and field intensity profiles for two fiber designs, where air-holes are running down their length, are investigated using plane-wave expansion theory and a variational principle [12]–[14].

The starting point is the fully vectorial wave equation for the complex magnetic field $\mathbf{H}(\mathbf{r})$, i.e.

$$\nabla \times \left(\frac{1}{\varepsilon_r(\mathbf{r})} \nabla \times \mathbf{H}(\mathbf{r}) \right) = \frac{\omega^2}{c^2} \mathbf{H}(\mathbf{r}). \quad (1)$$

This wave equation is treated as a Hermitian eigenvalue problem, where \mathbf{H} represents the eigenvector and ω^2/c^2 is the corresponding eigenvalue. The structures considered are defined by the dielectric function $\varepsilon_r(\mathbf{r})$, and in this paper the fiber designs in concern will be approximated with a dielectric function characterized by discrete translational symmetry in the x – y plane and invariance in the z -direction. This technique is often referred to as a supercell approximation. The fiber designs considered in this paper are shown in Fig. 1. To the left is shown a fiber design, where air-holes running down the length of the fiber are arranged in a honeycomb pattern. A waveguide has been created by introducing an extra air-hole in the structure. The supercell used in this paper as an approximation of the honeycomb fiber is shown with a dashed line. The honeycomb fiber design considered in this paper is characterized by a hole-diameter to hole-spacing ratio $D_H/\Lambda_H = 0.41$ that yields a large out-of-plane photonic bandgap [9], and the extra air-hole introduced to create a waveguide has the same size as the other air-holes. To the right is shown a design where

Manuscript received July 21, 1999; revised January 17, 2000. This work was supported by the Danish Technical Research Council under the THOR (Technology by Highly Oriented Research) Program.

The author is with the Research Center COM, Technical University of Denmark, DK-2800 Lyngby, Denmark (e-mail: ts@com.dtu.dk).

Publisher Item Identifier S 0733-8724(00)03042-5.

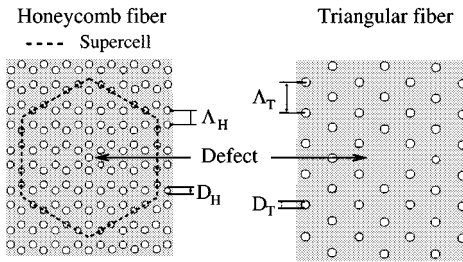


Fig. 1. Illustration of two fiber designs, where air-holes are running down the length of the fiber. To the left is shown the honeycomb fiber, where air-holes are arranged in a honeycomb pattern. A waveguide is created by introducing a defect in the structure, i.e., by introducing an extra air-hole. To the right is shown a design where air-holes are arranged on a triangular lattice. In this case a waveguide is created by removing one of the air-holes. The supercell used for modeling the honeycomb fiber design in this paper is shown with a dashed line.

air-holes are arranged on a triangular lattice. In this case, a waveguide has been created by removing a single air-hole. An air-hole diameter to hole-spacing ratio $D_T/\Lambda_T = 0.23$ being small enough for the fiber to be endlessly single-moded [1] has been chosen for this design. This choice makes possible single-moded fibers with large core areas. Smaller ratios D_T/Λ_T may be chosen as was done in [4], however, very small ratios D_T/Λ_T result in poor localization of the guided modes to the core region. Note that the triangular fiber may also be considered for obtaining small mode areas by choosing large ratios D_T/Λ_T as was done in [20]. In this case, however, limitations in the single-mode range of wavelengths becomes an important issue. The two chosen fiber designs are as will be shown single-moded for the frequency ranges of interest.

For structures characterized by discrete translational symmetry, a solution may, according to Bloch's theorem, be written as a plane wave modulated by a function U characterized by the same discrete translational symmetry as the structure itself. The function U is approximated with a Fourier-series expansion in terms of reciprocal lattice vectors G leading to the following expression for the solutions

$$H_{\mathbf{k},n}(\mathbf{r}) = \sum_{\mathbf{G}} \sum_{\lambda=1,2} \mathbf{h}_{\mathbf{k},\mathbf{G},\lambda,n} e^{i(\mathbf{k}+\mathbf{G}) \cdot \mathbf{r}} \quad (2)$$

where \mathbf{k} is a wave-number vector and λ represents the two field directions perpendicular to $\mathbf{k} + \mathbf{G}$. The set of discrete solutions for a given wave number vector \mathbf{k} , on the form (2), are organized after increasing eigenvalues ω^2/c^2 using the band number n . The solutions (2) are found using a variational method based on minimization of the functional

$$E(\mathbf{H}) = \frac{\left\langle \nabla \times \left(\frac{1}{\varepsilon_r(\mathbf{r})} \nabla \times \mathbf{H} \right) \mathbf{H} \right\rangle}{\langle \mathbf{H} | \mathbf{H} \rangle}. \quad (3)$$

When this functional is at a minimum the argument \mathbf{H} is an eigenvector and $E(\mathbf{H})$ is the corresponding eigenvalue. By inserting a trial vector on the form (2) in (3), the functional effectively becomes a function of the coefficients $\mathbf{h}_{\mathbf{k},\mathbf{G},\lambda,n}$, and the problem is reduced to varying these coefficients along a path that minimizes the functional. An efficient iterative approach that performs this task is described in [14]. Higher order solutions are found by restricting the trial-vectors to be orthogonal

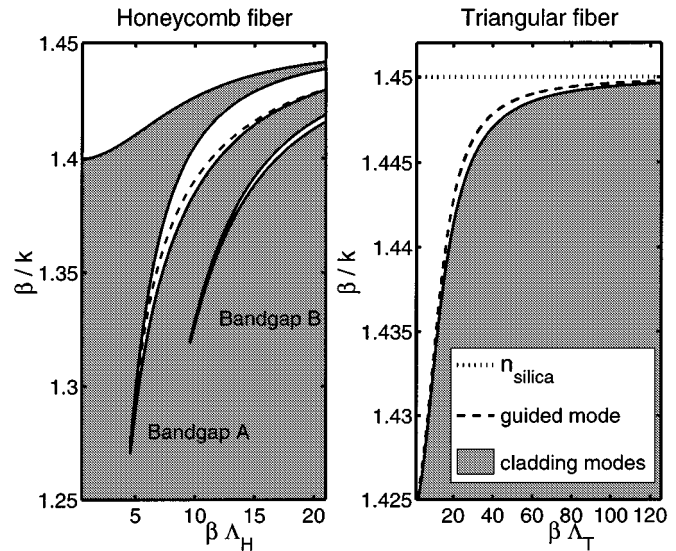


Fig. 2. The figure shows the continuum of allowed $(\beta/k, \beta\Lambda)$ in the cladding structures surrounding the core in the honeycomb fiber and the triangular fiber, where β is the out-of-plane wave vector component, k is the free-space wave number and $\Lambda = \Lambda_H, \Lambda_T$ are the center-to-center hole-spacings in the cladding structures for the honeycomb fiber and the triangular fiber, respectively. The white regions represent values for $(\beta/k, \beta\Lambda)$ that are not allowed in the cladding structure, and the dashed lines correspond to guided modes that are localized to the fiber-core region. The dotted line represents the refractive index of silica used for the calculation.

to all previously found eigenvectors and using the same minimization principle. The computer memory requirements using this method scales linearly with the number of plane waves N used in the expansion (2), whereas the required computer calculation time scales as $N \log N$. A large number of plane waves N are required for accurate modeling of the structures considered in this paper, and it is exactly for large numerical problems that this method is numerically efficient compared to previous plane wave expansion methods [21]. More details regarding the method may be found in [12].

The single-mode properties of the two chosen fiber designs are illustrated in Fig. 2. The figure shows for both fiber designs the continuum of allowed $(\beta/k, \beta\Lambda)$ for cladding modes, where β is the out-of-plane wave vector component, k is the free-space wave number, and $\Lambda = \Lambda_H, \Lambda_T$ are the center-to-center hole-spacings in the cladding structures for the honeycomb fiber and the triangular fiber, respectively. The honeycomb fiber is unique in the sense that light is localized to a region near where the refractive index has been decreased relative to the surrounding structure, i.e., a region where an extra air-hole has been introduced. Therefore light is not guided by the principle of total internal reflection but is guided by the photonic bandgap effect [6]. This is possible due to the existence of out-of-plane photonic bandgaps such as bandgaps A and B in Fig. 2, where cladding modes are not allowed. The dashed line in bandgap A for the honeycomb fiber and the dashed line above the continuum of cladding modes for the triangular fiber correspond to two doubly degenerate guided modes being localized to the fiber-core region (the defect shown in Fig. 1).

Since no guided modes appear in bandgap B the honeycomb fiber is single-moded for the considered wavelength range corresponding to the dashed line in bandgap A. This does not have

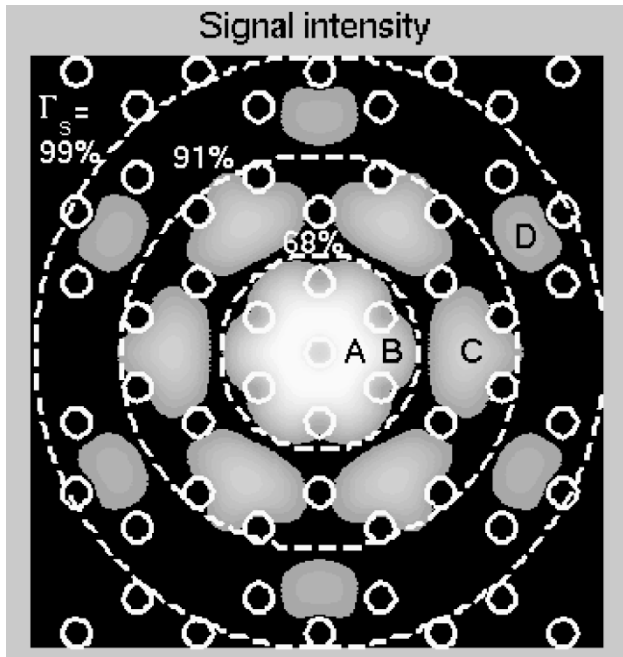


Fig. 3. Intensity profile for the signal (1560 nm) in the honeycomb fiber with hole-spacing $\Lambda_H = 1.62 \mu\text{m}$ and hole-diameter to hole-spacing ratio $D_H/\Lambda_H = 0.41$. Along with the intensity profile the contour of the structure is plotted (solid lines). Three circles are plotted (dotted lines) along with the fraction Γ of the mode energy within this circle. The intensity profile has been calculated using 256×256 plane waves. Four locations have been labeled A, B, C, and D.

to be true in general for the honeycomb fiber for other choices of hole-diameter to hole-spacing ratios D_H/Λ_H and other choices of the size of the defect air-hole. Since only two degenerate modes appear above the continuum of cladding modes for the triangular fiber, this fiber is also single-moded for the wavelength range corresponding to the dashed line, i.e., this fiber is single-moded for normalized frequencies $\Lambda_T/\lambda_0 < 126/(1.45 \cdot 2\pi) = 13.8$, at least.

The wavelengths of interest are 980 and 1560 nm, and a hole spacing Λ_H must be chosen so that guided modes exist and are well-localized at both wavelengths for the honeycomb fiber. For this reason $\Lambda_H = 1.62 \mu\text{m}$ has been chosen, and for this choice Fig. 3 shows the field intensity profile for the wavelength 1560 nm. With this choice of Λ_H the wavelength 1560 nm corresponds to $\beta\Lambda_H = 9$, whereas 980 nm corresponds to $\beta\Lambda_H = 14.3$. In Fig. 3 three dotted circles have been plotted along with the fraction Γ_s of the signal energy confined within the circle.

A similar plot of the field intensity profile at 980 nm does not look much different. In that case the energy confined within the same three circles is $\Gamma_p = 99$, $\Gamma_p = 93$, and $\Gamma_p = 73\%$, respectively. Note that for a standard step index fiber being single-moded at both 1560 and 980 nm less than 50% of the mode energy is confined to the core region for the mode at 1560 nm. The differences between pump (980 nm) and signal (1560 nm) are more clearly seen by comparing the cross-sectional plots shown in Fig. 4. From Fig. 4 is seen that some signal energy is present in the defect air-hole, whereas almost no pump energy is present in the defect air-hole. The intensity profiles may be used to get an understanding of where erbium doped fiber lasers based on the

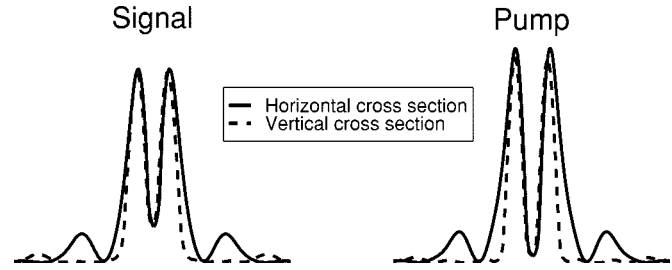


Fig. 4. Cross sectional plot of signal and pump intensity.

honeycomb photonic crystal fiber should be doped with erbium. Naturally, the erbium should be placed in such a way that both the signal intensity distribution and the pump intensity distribution are of significant amplitude at the position of the erbium.

The field intensity profile for the triangular photonic crystal fiber is shown to the left in Fig. 5 for the fundamental guided mode characterized by the normalized frequency $\Lambda_T/\lambda_0 = 8.8$, where λ_0 is the free-space wavelength. In Fig. 5 (right) vertical and horizontal cross sections of the field intensity profile through the center of the fiber core for a number of normalized frequencies Λ_T/λ_0 are shown, where Λ_T is kept constant. Clearly the distribution of the mode intensity at the center does not change much with frequency for high frequencies, whereas more significant changes are seen with frequency for low frequencies.

III. MODELING PHOTONIC CRYSTAL DISTRIBUTED FEEDBACK FIBER LASERS WITH BRAGG GRATINGS

In Section III a model for distributed feedback Er^{3+} -doped fiber lasers is presented. Steady-state solutions are calculated using a transfer-matrix method [17], [18] based on coupled-wave theory [16] and a model for gain provided by Er^{3+} pumped with 980 nm light [19]. The model for gain takes into account the spatial distribution of Er^{3+} relative to the spatial mode intensity distribution at the signal and pump wavelengths, respectively. In [18] gain was calculated using a one-dimensional approach based on confinement factors and the assumption that the inversion of the gain medium Er^{3+} is constant across the fiber cross section. Whereas this is an excellent approximation for standard step-index fiber doped uniformly within the core region this assumption is not valid in general near threshold for more complicated doping profiles and mode intensity profiles.

A distributed feedback waveguide may be created by introducing a spatial periodic modulation of the refractive index in the z -direction of a fiber. In this paper the simple case of a sinusoidal refractive index modulation is considered, i.e.

$$n(z) = n_0 + \Delta n \sin(2\beta_B z + \phi) \quad (4)$$

where

n_0 average refractive index;

Δn amplitude of the index modulation;

β_B Bragg wave number.

For wave propagation vectors β close to β_B there will be two counter-running waves with complex amplitudes $E_+(z)$ and $E_-(z)$ coupled by backward Bragg scattering. Consider a short

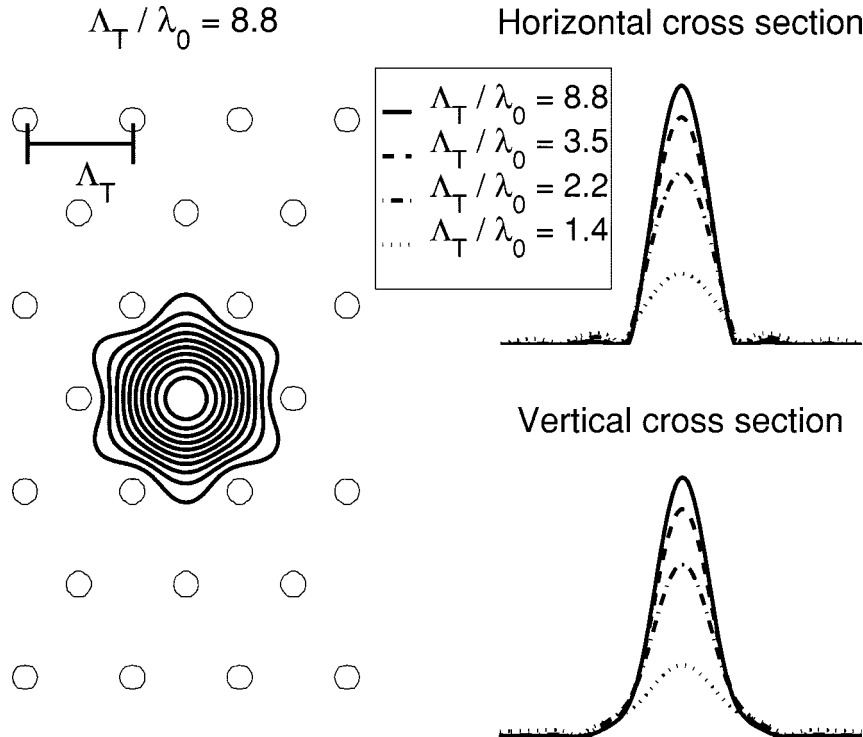


Fig. 5. To the left is shown a contour plot of the field intensity profile in a photonic crystal fiber corresponding to the normalized frequency $\Lambda_T/\lambda_0 = 8.8$, where Λ_T is shown in the figure and λ_0 is the free-space wavelength. To the right is shown horizontal and vertical cross sections of the field intensity profile for a number of frequencies Λ_T/λ_0 , where Λ_T is kept constant.

section of distributed feedback waveguide of length Δz where n_0 , Δn , β_B , and gain g provided by Er^{3+} may be assumed constant. By further assuming the gain over one grating period to be small, i.e., $g \ll \beta_B$, and the index modulation to be a small perturbation, i.e., $\Delta n \ll n_0$, the following coupled wave equations may be obtained

$$\frac{dE_+}{dz} = \kappa e^{i(2\Delta\beta z - \phi)} E_- + \frac{g}{2} E_+ \quad (5)$$

$$\frac{dE_-}{dz} = \kappa e^{-i(2\Delta\beta z - \phi)} E_+ - \frac{g}{2} E_- \quad (6)$$

where $\Delta\beta = \beta - \beta_B$. The coupling coefficient κ is given by $\kappa = 2\pi\Delta n/\lambda_0$. If the complex amplitudes E_+ and E_- are known at some position z these coupled equations may be solved to provide the corresponding amplitude at any position $z + \Delta z$. The amplitudes at position $z + \Delta z$ are related to the amplitudes at position z by the following transfer matrix [17]

$$\begin{pmatrix} E_{s,+}(z + \Delta z) \\ E_{s,-}(z + \Delta z) \end{pmatrix} = \begin{pmatrix} F_{11} & F_{12} \\ F_{21} & F_{22} \end{pmatrix} \begin{pmatrix} E_{s,+}(z) \\ E_{s,-}(z) \end{pmatrix} \quad (7)$$

where the elements of the transfer matrix are given by

$$\begin{aligned} F_{11} &= \left(\cosh(\gamma\Delta z) - i\frac{\Delta\beta'}{\gamma} \sinh(\gamma\Delta z) \right) e^{-i\beta_B\Delta z}, \\ F_{12} &= \frac{\kappa}{\gamma} \sinh(\gamma\Delta z) e^{i(\beta_B\Delta z - \phi)}, \\ F_{21} &= \frac{\kappa}{\gamma} \sinh(\gamma\Delta z) e^{-i(\beta_B\Delta z - \phi)}, \\ F_{22} &= \left(\cosh(\gamma\Delta z) + i\frac{\Delta\beta'}{\gamma} \sinh(\gamma\Delta z) \right) e^{i\beta_B\Delta z} \end{aligned} \quad (8)$$

where $\Delta\beta' = \Delta\beta + ig/2$, $\gamma^2 = \kappa^2 - (\Delta\beta')^2$ and ϕ is the phase of the grating at position z .

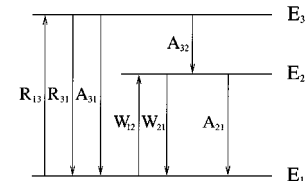


Fig. 6. Energy level diagram for a three-level gain medium.

In this paper we consider gain g provided by Er^{3+} pumped with 980 nm light, and in this case Er^{3+} may be considered a three-level gain medium [19]. The energy level diagram for a three-level gain medium is shown in Fig. 6. Absorption and stimulated emission is denoted in the diagram by the letters R and W , where R represents transitions at the pump wavelength, whereas W represents transitions at the laser wavelength. Spontaneous decay is denoted by the letter A . The spontaneous decay from the energy level E_2 is usually expressed by the lifetime τ , i.e., $A_{21} = 1/\tau$. In this paper the lifetime τ is set equal to 10 ms. Note that the effect of up-conversion on the lifetime is neglected.

By assuming $A_{32} \gg R_{13,31}$ and $A_{32} \gg A_{31}$ [19] the population at the energy level E_3 is negligible. The fraction of the Er^{3+} at the energy level E_2 is referred to as the inversion X . The inversion X is given by

$$X = \frac{R_{13}\tau + W_{12}\tau}{1 + R_{13}\tau + W_{12}\tau + W_{21}\tau}. \quad (9)$$

The transition rates R_{13} , W_{12} and W_{21} are given by the following expressions:

$$R_{13} = \sigma_{a,p} f_p(\mathbf{r}) n_p \quad (10)$$

$$W_{12} = \sigma_{a,s} f_s(\mathbf{r}) n_s \quad (11)$$

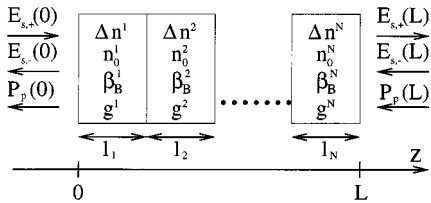


Fig. 7. Diagram of a waveguide with Bragg gratings divided in N segments with constant parameters β_B , n_0 , Δn , and g . The waveguide structure is pumped from the right end with the pump power $P_p(L)$. The complex amplitudes of the forward propagating wave $E_{s,+}(0)$ and the backward propagating wave $E_{s,-}(0)$ are illustrated at the two ends of the waveguide.

$$W_{21} = \sigma_{a,p} f_s(\mathbf{r}) n_s \quad (12)$$

where $\sigma_{a,p}$ is the absorption cross section at the pump wavelength and $\sigma_{a,s}$ and $\sigma_{e,s}$ are the absorption and emission cross sections at the signal wavelength. The terms $f_s(\mathbf{r})$ and $f_p(\mathbf{r})$ represent the intensity distribution for signal and pump, respectively. The intensity distributions are defined by

$$f_i(\mathbf{r}) = \frac{\varepsilon_r(\mathbf{r}) |\mathbf{E}_i(\mathbf{r})|^2}{\int \varepsilon_r(\mathbf{r}) |\mathbf{E}_i(\mathbf{r})|^2 d^2\mathbf{r}}, \quad i = s, p. \quad (13)$$

The intensity distribution (13) is shown for the honeycomb fiber in Figs. 3 and 4, and for the triangular fiber design in Fig. 5.

The parameter n_p represent pump photons per unit time, whereas $n_s = n_{s,+} + n_{s,-}$ represent the sum of signal photons per unit time in the forward propagating wave $n_{s,+}$ and in the backward propagating wave $n_{s,-}$.

The effective gain per unit length, expressed in terms of the inversion $X(\mathbf{r})$, the mode intensity profiles $f_s(\mathbf{r})$, $f_p(\mathbf{r})$, the cross sections $\sigma_{a,p}$, $\sigma_{a,s}$, and $\sigma_{e,s}$ and background losses α_s , α_p , for signal ($g_s(z)$) and pump ($g_p(z)$) is given by (14) and (15)

$$g_s(z) = \int \rho(\mathbf{r}) f_s(\mathbf{r}) (X(\mathbf{r}) \sigma_{e,s} - (1 - X(\mathbf{r})) \sigma_{a,s}) d^2\mathbf{r} - \alpha_s \quad (14)$$

$$g_p(z) = - \int \rho(\mathbf{r}) f_p(\mathbf{r}) (1 - X(\mathbf{r})) \sigma_{a,p} d^2\mathbf{r} - \alpha_p. \quad (15)$$

In erbium lasers with Bragg gratings n_0 , Δn , β_B , and g may vary along the fiber axis. In order to be able to use the transfer matrix (7) the waveguide is divided into N segments with constant parameters β_B , n_0 , Δn , and g . This is illustrated in Fig. 7. In Fig. 7 the amplitudes $E_{s,+}$ and $E_{s,-}$ of forward and backward propagating waves are shown at the two ends of the distributed feedback waveguide. In lasers there is no in-going signal field at the two ends of the fiber. Therefore the boundary conditions that must be fulfilled are $E_{s,+}(0) = E_{s,-}(L) = 0$. For a given pumped erbium waveguide with Bragg gratings a solution is defined by two parameters β and $E_{s,+}(L)$ for which this boundary condition is satisfied. The calculation starts by assuming a value for $E_{s,+}(L)$ and β . Using the boundary condition $E_{s,-}(L) = 0$ the amplitude of both forward and backward propagating waves are known at position $z = L$. By using the expression (14) the gain g is determined for segment N . Using this gain and the transfer matrix (7) the

complex amplitudes at the interface to the next segment (position $z = L - l_N$) are found. The pump power present at the interface to the next segment is determined using expression (15) for the pump gain g_p and

$$\frac{dP_p}{dz} = g_p P_p. \quad (16)$$

By repeating this procedure the complex amplitudes $E_{s,+}(0)$ and $E_{s,-}(0)$, at the left end of the waveguide, are found. The parameters β and $E_{s,+}(L)$ are adjusted using linear interpolation until the boundary condition $E_{s,+}(0) = 0$ is fulfilled.

IV. NUMERICAL RESULTS FOR ERBIUM-DOPED PHOTONIC CRYSTAL DISTRIBUTED FEEDBACK FIBER LASERS

In Section IV numerical results are presented for two erbium-doped fiber laser designs, where the fibers have air-holes running down the length of the fiber.

The first fiber laser design, we will consider is based on the honeycomb photonic crystal fiber described in Section II. It is assumed that a periodic sinusoidal index modulation is created along 5 cm of the length of the fiber using UV exposure, and that a grating phase shift $\Delta\phi = \pi$ is created at the center of the grating. The writing of a Bragg grating in fibers with air-holes using ultraviolet light requires further study. The problem that might be faced here is to overcome technical problems in writing the Bragg grating due to scattering of the ultraviolet light by the air-holes. This problem will not be investigated in this paper.

In Section II, a field intensity profile was given for the signal with wavelength 1560 nm, and circles denoted $\Gamma_s = 99$, 91, and 68% indicated circles within which 99, 91, and 68% of the mode energy was confined. In this section, we will consider honeycomb fiber lasers doped with the erbium concentration $\rho = 1.74 \cdot 10^{25} \text{ m}^{-3}$ within each of these three circles. This will provide an idea of the behavior of the fiber for different choices of erbium-doped regions in the fiber. The emission and absorption is modeled using the emission and absorption cross sections $\sigma_{e,s} = 3.38 \cdot 10^{-25} \text{ m}^2$, $\sigma_{a,s} = 1.85 \cdot 10^{-25} \text{ m}^2$, and $\sigma_{a,p} = 2.53 \cdot 10^{-25} \text{ m}^2$.

Since the discrete phase shift of $\Delta\phi = \pi$ at the center of the grating was chosen the detuning $\Delta\beta$ is zero, and the period of the index modulation is, therefore, given by

$$\frac{\pi}{\beta_B} = \frac{\pi}{\beta} = \frac{\pi}{(\beta/k)} \frac{1}{k} = \frac{1}{2} \frac{\lambda_0}{(\beta/k)} \quad (17)$$

where λ_0 is the free-space wavelength. This leads to the period of the index-modulation of 565 nm. For a standard step-index fiber this period will be slightly smaller since the ratio β/k is higher.

First, we will consider for the honeycomb fiber laser the properties for a relatively high pump power of 100 mW. Fig. 8 shows output power from one end of the fiber as a function of modulation strength κ for the fixed pump power 100 mW. Clearly, if the modulation strength κ is too weak the output power is zero, i.e., there is no lasing. It is also clear that as the region doped with erbium is changed from a region covering $\Gamma_s = 68\%$ of the mode energy to a region covering 91% or 99% the fiber will lase at lower modulation strengths and provide more output power at a fixed modulation strength. In both cases this is due to the more

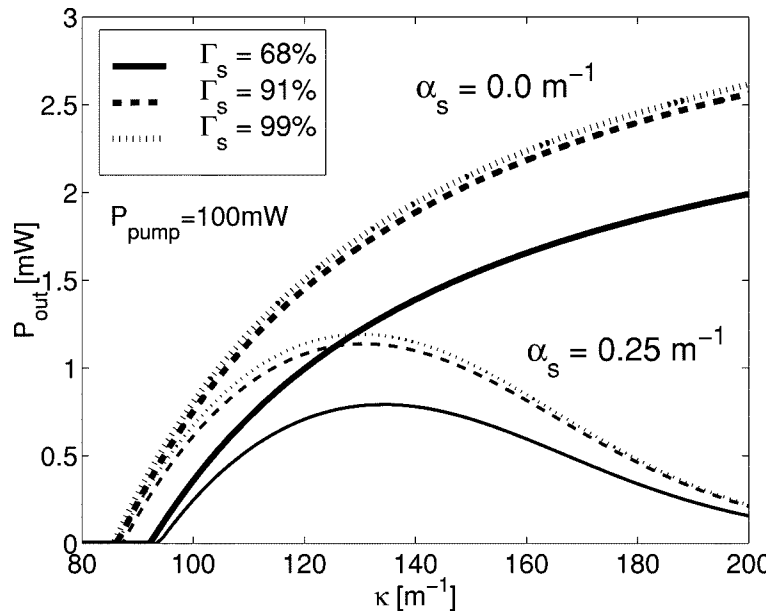


Fig. 8. Output power as a function of modulation strength κ for the honeycomb photonic crystal fiber with hole-spacing $\Lambda = 1.62 \mu\text{m}$ and hole-diameter to hole-spacing ratio $D/\Lambda = 0.41$. The defect hole has the same size as the other holes. The calculation has been performed for the fiber doped with the erbium concentration $\rho = 1.74 \cdot 10^{25} \text{ m}^{-3}$ within circles where 99, 91, and 68% of the signal power is confined. Both a fiber laser with no waveguide loss ($\alpha_s = 0.0 \text{ m}^{-1}$) and a fiber with waveguide loss and/or absorption loss ($\alpha_s = 0.25 \text{ m}^{-1}$) are considered.

erbium providing more gain. However, since the pump intensity profile at positions C and D has lower amplitude compared to the pump intensity profile at positions A and B (see Fig. 3), a high pump power is required for the erbium at positions C and especially D to have sufficient inversion to offer any reasonable amplification of the light.

In Fig. 8 both a case with no background loss (absorption / waveguide loss) denoted $\alpha_s = 0.0 \text{ m}^{-1}$ and a case with background loss denoted $\alpha_s = 0.25 \text{ m}^{-1}$ are considered. For the case with background losses taken into account there is an optimum modulation strength, where the output power is maximized, for the given pump power. If the modulation strength is higher than this optimum the output power decreases since relatively more light is lost due to the background losses compared to the useful light coupled out through the Bragg mirrors. Note that the optimum modulation strength depends on both background loss α_s and the length of the fiber laser.

The advantage of using a high modulation strength is, however, that the threshold pump power required for lasing will be lower.

The situation for pump powers near the pump threshold is illustrated in Fig. 9. Note that the slope of the curves in Fig. 9 is lower near threshold, a result which is seen only because the model for gain takes into account the spatial distribution and inversion of Er^{3+} relative to the signal and pump intensity across the fiber and along the fiber. Fig. 9 shows that the choice of doping within the $\Gamma_s = 68\%$ circle offers the lowest pump power threshold both when background losses are not present ($\alpha_s = 0.0 \text{ m}^{-1}$) and in the presence of background losses ($\alpha_s = 0.25 \text{ m}^{-1}$). As the area doped with erbium covers a larger fraction of the mode intensity profiles the pump power threshold increases. Note that whereas the output power is highest for the doped region covering 99% of the mode energy in Fig. 8, where

the pump power is high, this is not the case in Fig. 9 where the pump power is low.

The inversion at the four positions A, B, C, and D along the length axis of the fiber laser is shown for a high and a low pump power in Fig. 10. For the high pump power 100 mW the inversion at positions A, B, and C is approximately the same along the fiber. At position D the inversion is significantly lower relative to the other positions even at high pump powers. However, for the pump power 100 mW the inversion at position D is still sufficiently high for the erbium to provide amplification of the light. The low inversion at position D can be understood by noting that the amplitude of the signal intensity distribution $f_s(\mathbf{r})$ is high relative to the pump intensity distribution $f_p(\mathbf{r})$ at this position.

At the center of the fiber laser ($L_{\text{rel}} = 0.5$) the inversion is low relative to the inversion at the edges of the fiber laser. This is due to high signal power at the center of the structure. The signal power along the fiber is shown as an inset in Fig. 10. The inversion at the same four positions for the pump power 5 mW only slightly above threshold is shown to the right in Fig. 10. In this case the inversion at position D is below $\sigma_{a,s}/(\sigma_{a,s} + \sigma_{e,s}) = 0.35$, and erbium at this position will attenuate the signal. The inversion at position D peaks at the center of the fiber laser ($L_{\text{rel}} = 0.5$), where the signal intensity peaks, as a consequence of the absorption of the signal. Also note that the asymmetry seen in Fig. 10 is due to the fiber being pumped from the right end.

The large mode-area fiber with circular air-holes arranged on a triangular lattice with a single air-hole removed hold both advantages and disadvantages. Here we will again consider a fiber design of length 5 cm with a UV-induced Bragg grating with a phase shift of $\Delta\phi = \pi$ at the center of the grating. We choose the same erbium concentration and emission / absorption cross

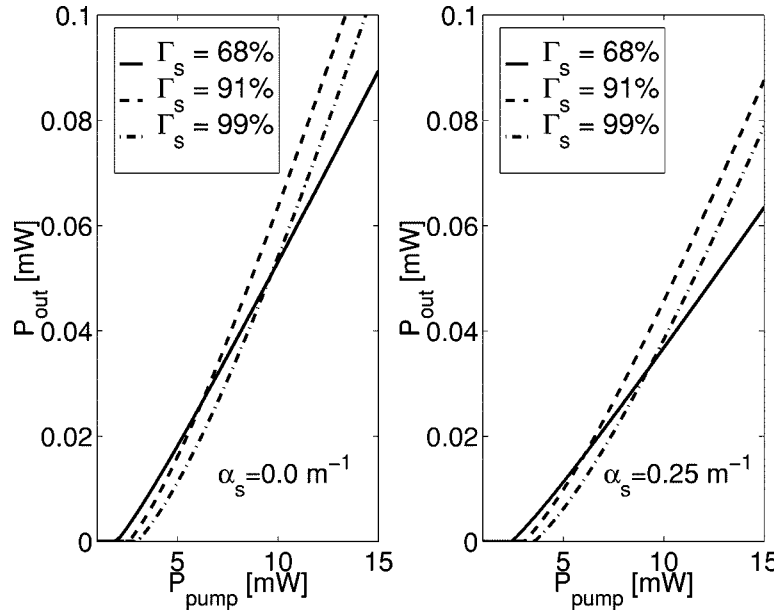


Fig. 9. Output power as a function of pump power for the erbium doped honeycomb photonic crystal fiber laser with modulation strength $\kappa = 110 \text{ m}^{-1}$. The calculation has been performed for the fiber doped with the erbium concentration $\rho = 1.74 \cdot 10^{25} \text{ m}^{-3}$ within a region covering 99, 91, and 68% of the signal power. To the left is shown a calculation where background losses α_s are set equal to 0, whereas the calculation to the right takes into account a background loss of $\alpha_s = 0.25 \text{ m}^{-1}$.

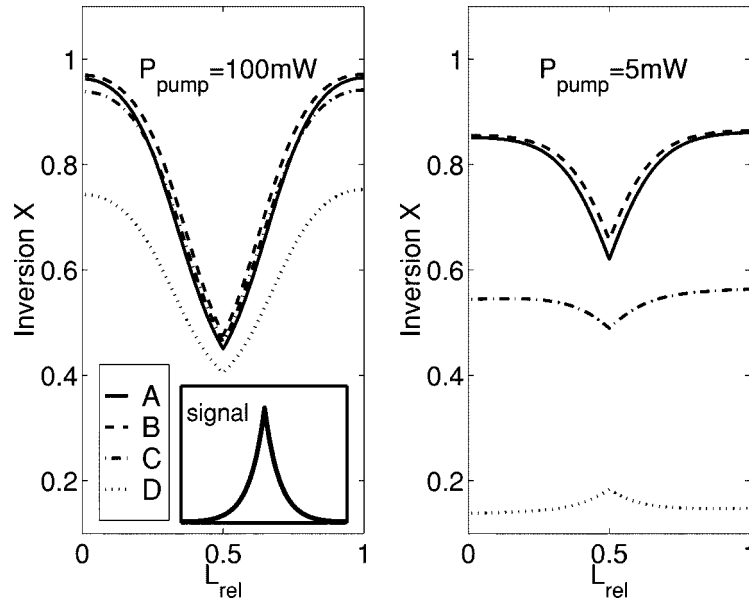


Fig. 10. Inversion at four positions A, B, C, and D in the erbium doped honeycomb distributed feedback fiber laser for two choices of pump power. Left: a high pump power of 100 mW and right: a pump power of 5 mW only slightly above threshold. The inset shows the sum of signal powers in forward and backward running waves.

sections that were also used above for modeling the honeycomb fiber laser.

The disadvantage of using large-mode area fibers for fiber lasers is that in order to achieve the same amplification per unit length a larger area must be doped with Er^{3+} . This leads to significant losses due to spontaneous emission and consequently a higher pump power threshold. This is illustrated in Fig. 11 for the erbium-doped triangular photonic crystal distributed feedback fiber laser for three sizes of fibers given by the center-to-center hole-spacing Λ_T . The region doped with Er^{3+} is shown

with a circle in the inset. The fraction of signal and pump energy within the circle in the inset for all three choices of Λ_T are in the range from 84–88%. Fig. 11 shows that for a relatively modest size of fiber core given by the center-to-center hole-spacing $\Lambda_T = 3.4 \mu\text{m}$ the pump power threshold of 5.0 mW is certainly higher than what was the case for the honeycomb fiber, even for the honeycomb fiber doped within a large region covering 99% of the mode energy. This difference is due to the small effective mode area of the honeycomb fiber laser. As the size of the triangular fiber is increased to $\Lambda_T = 5.4 \mu\text{m}$ the area doped with

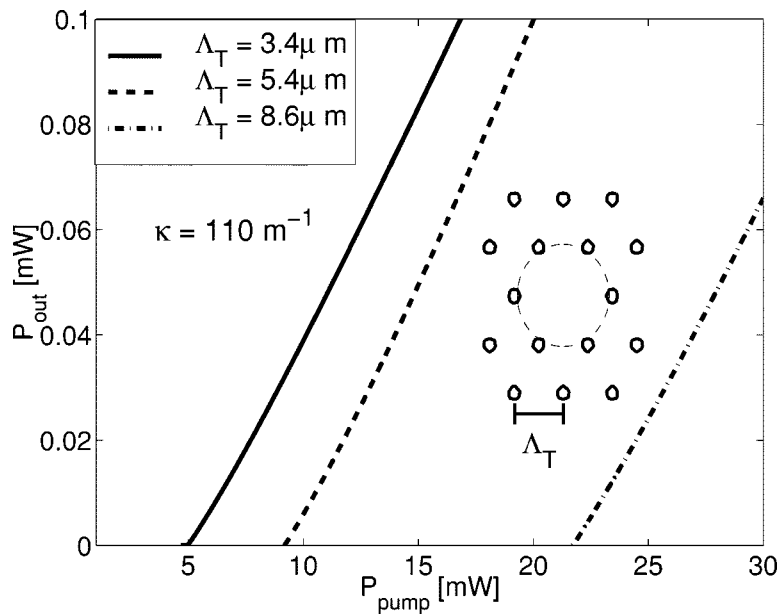


Fig. 11. Illustration of pump power threshold for three sizes of erbium-doped triangular photonic crystal distributed feedback fiber lasers. The size parameter Λ_T represents the center-to-center hole-spacing in the fiber design.

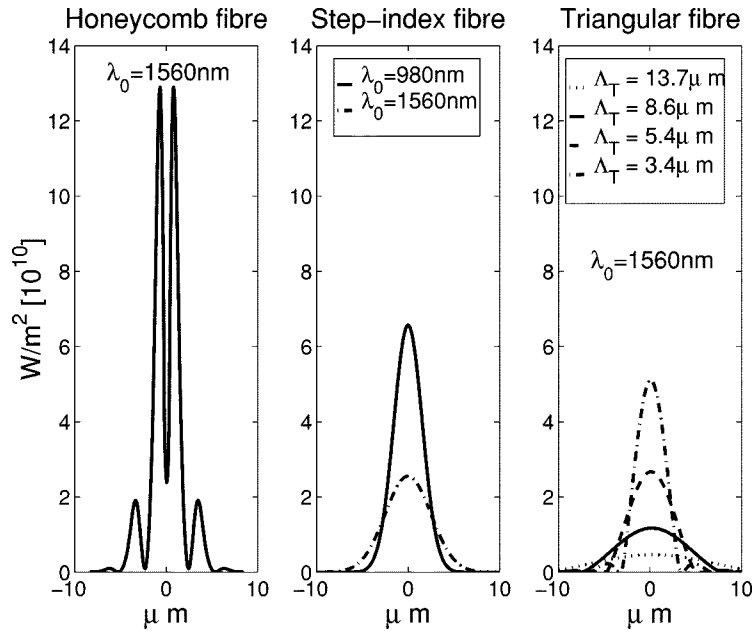


Fig. 12. The figure shows local intensity in units W/m^2 for the honeycomb photonic crystal fiber, the standard step-index fiber and the triangular photonic crystal fiber, where the total power passing through the fibers is 1 W.

Er^{3+} increases, and consequently the pump power threshold increases to 9.2 mW. For $\Lambda_T = 8.6 \mu\text{m}$ the pump power threshold has increased to 21.7 mW.

The advantage of the triangular photonic crystal fiber laser is, however, not found near the pump power threshold. This fiber is suitable for high power applications. In Fig. 12 the local intensity (W/m^2) for the signal is shown for the honeycomb photonic crystal fiber, the standard step-index fiber and the triangular photonic crystal fiber. In all cases the total power passing through the fiber is assumed to be 1 W. The local intensity profile for a standard step-index fiber shown in Fig. 12 has been

calculated by assuming a Gaussian distribution function and a core with radius 2 μm . The wavelength 980 nm is chosen as the single-mode cut-off wavelength, i.e., for shorter wavelengths the step-index fiber is multimoded. The peak amplitudes at 1560 and 980 nm for the step-index fiber are considerably different. This is not the case for the guided modes at the same two wavelengths in the honeycomb fiber design (see Fig. 4).

As the area increases for the triangular photonic crystal fiber the local intensity may become very low for the same total transmitted intensity relative to other fiber designs. This makes possible higher output powers and pump powers before the glass at

the center of the fiber laser, where the signal intensity is high, melts. Furthermore, higher powers are possible before the performance is limited by intensity-dependent nonlinear effects.

V. CONCLUSION

Two photonic crystal fiber designs, with circular air-holes running down the length of the fiber, have been considered for making erbium-doped distributed feedback fiber lasers with Bragg gratings. Both photonic crystal fiber designs are single-moded at the signal wavelength 1560 nm and the pump wavelength 980 nm.

The mode intensity profiles at the two wavelengths 1560 and 980 nm differs only slightly for the honeycomb photonic crystal fiber design. This is also the case for the triangular photonic crystal fiber design when the wavelengths 1560 and 980 nm are both small compared to the dimensions of the microstructure in the fiber. Both properties, i.e., single-moded at 1560 and 980 nm and only a small deviation between the mode intensity distributions at these two wavelengths, is not possible in standard step-index fiber. The honeycomb fiber is characterized by having a large fraction of the mode energy confined within a small area, whereas the triangular photonic crystal fiber is characterized by large mode areas. This difference leads to small pump power thresholds and high local peak intensities (W/m^2) for the honeycomb photonic crystal fiber laser, whereas high powers are possible in the large-mode-area triangular photonic crystal fiber laser before the performance is limited by heating effects and intensity-dependent nonlinear effects.

ACKNOWLEDGMENT

The author would like to thank J. Broeng, S. E. Barkou, and A. Bjarklev for their helpful discussions.

REFERENCES

- [1] T. A. Birks, J. C. Knight, and P. S. Russell, "Endlessly single-mode photonic crystal fiber," *Opt. Lett.*, vol. 22, no. 13, pp. 961–963, July 1997.
- [2] J. C. Knight, T. A. Birks, P. S. J. Russell, and D. M. Atkin, "All-silica single-mode optical fiber with photonic crystal cladding," *Opt. Lett.*, vol. 21, no. 19, pp. 1547–9, Oct. 1996.
- [3] J. C. Knight, T. A. Birks, P. S. J. Russell, and J. P. Sandro, "Properties of photonic crystal fiber and the effective index model," *J. Opt. Soc. Amer. A*, vol. 15, no. 3, pp. 748–52, March 1998.
- [4] J. C. Knight, T. A. Birks, R. F. Cregan, P. S. J. Russell, and J.-P. de Sandro, "Large mode area photonic crystal fibre," *Electron. Lett.*, vol. 34, no. 13, pp. 1347–1348, June 1998.
- [5] J. C. Knight, J. Broeng, T. A. Birks, and P. S. J. Russell, "Photonic band gap guidance in optical fibers," *Science—AAAS—Weekly Paper Edition*, vol. 282, no. 5393, pp. 1476–1477, 1998.
- [6] J. Broeng, T. Søndergaard, S. E. Barkou, P. M. Barbeito, and A. Bjarklev, "Waveguidance by the photonic bandgap effect in optical fibres," *J. Opt. A: Pure Appl. Opt.*, vol. 1, no. 4, pp. 477–82, 1999.
- [7] P. J. Bennett, T. M. Monro, and D. J. Richardson, "A robust, large air fill fraction holey fibre," in *Proc. CLEO'99*, May 23–28, 1999, paper CWF64.
- [8] B. J. Mangan, J. C. Knight, and T. A. Birks, "Dual-core photonic crystal fibre," in *Proc. CLEO'99*, May 23–28, 1999, p. JFB8.
- [9] J. Broeng, S. E. Barkou, A. Bjarklev, J. C. Knight, T. A. Birks, and P. S. J. Russell, "Highly increased photonic band gaps in silica/air structures," *Opt. Commun.*, vol. 156, pp. 240–244, Nov. 1998.
- [10] S. E. Barkou, J. Broeng, and A. Bjarklev, "Silica-air photonic crystal fiber design that permits waveguiding by a true photonic bandgap effect," *Opt. Lett.*, vol. 24, no. 1, pp. 46–48, Jan. 1999.
- [11] A. Bjarklev, J. Broeng, K. Dridi, and S. Barkou, "Dispersion properties of photonic crystal fibres," in *Proc. 24th European Conf. Opt. Commun., ECOC'98*, vol. 1, Sept. 20–24, 1998, pp. 135–36.
- [12] R. D. Meade, A. M. Rappe, K. D. Brommer, J. D. Joannopoulos, and O. L. Alerh, "Accurate theoretical analysis of photonic band-gap materials," *Phys. Rev. B*, vol. 48, no. 11, pp. 8434–8437, September 1993.
- [13] ———, "Erratum: Accurate theoretical analysis of photonic band-gap materials," *Phys. Rev. B*, vol. 55, no. 23, p. 15942, June 1997.
- [14] M. P. Teter, M. C. Payne, and D. C. Allan, "Solution of Schrödinger's equation for large systems," *Phys. Rev. B*, vol. 40, no. 18, pp. 12 255–12 263, Dec. 1989.
- [15] A. Ferrando, E. Silvestre, J. J. Miret, and P. Andrés, "Full-vector analysis of a realistic photonic crystal fiber," *Opt. Lett.*, vol. 24, no. 5, pp. 276–278, Mar. 1999.
- [16] H. Kogelnik and C. V. Shank, "Coupled-wave theory of distributed feedback lasers," *J. Appl. Phys.*, vol. 43, no. 5, pp. 2327–2335, May 1972.
- [17] M. Yamada and K. Sakuda, "Analysis of almost-periodic distributed feedback slab waveguides via a fundamental matrix approach," *Appl. Opt.*, vol. 26, no. 16, pp. 3473–3478, August 1987.
- [18] V. C. Lauridsen, T. Søndergaard, P. Varming, and J. H. Povlsen, "Design of distributed feedback fibre lasers," in *Proc. 11th Int. Conf. Integr. Opt. Optic. Fibre Commun. 23rd European Conf. Optic. Commun. IOOC-ECOC 97, (Conf. Publ.)*, vol. 3, 1997, pp. 39–42.
- [19] E. Desurvire, *Erbium-Doped Fiber Amplifiers*. New York: Wiley, 1994.
- [20] K. R. Jinendra, R. S. Windeler, and A. J. Stentz, "Efficient visible continuum generation in air-silica microstructure optical fibers with anomalous dispersion at 800nm," in *Proc. CLEO'99*, May 23–28, 1999, paper CPD8-1, p. .
- [21] K. M. Ho, C. T. Chan, and C. M. Soukoulis, "Existence of a photonic gap in periodic dielectric structures," *Phys. Rev. Lett.*, vol. 65, no. 25, pp. 3152–5, Dec. 1990.



Thomas Søndergaard received the M.Sc.E.E degree from the Technical University of Denmark in March 1999. He is currently pursuing the Ph.D. degree in electrical engineering at Research Center COM at the Technical University of Denmark, where his work involves modeling of interaction between matter and light in active structures.